Analysis and Validation of a Novel Symmetrical Structure for Toroidal Variable Power Inductors in Energy Storage Systems

Sarah Saeed, *Member, IEEE,* and Jorge Garcia, *Senior Member, IEEE*.

***Abstract*—This paper presents an analysis of an alternative variable inductor structure compared to the ones previously proposed in the literature. The inductor is constructed based on a toroidal core and presents some prosperous advantages, which are: a reduced induced voltage in the DC bias control windings, and a symmetrical operation, while making use of the simplicity of a toroidal magnetic core. The proposed variable inductor topology is applied to a specific case study: the design and implementation of a bidirectional boost converter for integration of Battery Energy Storage Systems into DC grids. The variation of the inductance in this application provides an extra degree of freedom in the design which offers twofold improvement to the controlled system. On the one hand, it allows the system to keep the same impedance throughout the operation range. This guarantees that the behavior of the controlled system will remain the same and avoids the need to change the controller tuning and parameters each time the State-Of-Charge of the battery varies. And on the other hand, it enables control over the voltage and current ripple through the battery without the need to install extra capacitor banks. The design, assessment, and experimental procedures of the proposed variable inductor structure for this application case are shown in this paper. The results show an improvement in the performance of the selected case study.**

***Index Terms*—Variable inductor, distributed airgap, controlled saturation, iron powder, energy storage systems, power electronic converters.**

I. INTRODUCTION

VARIABLE magnetic elements are electromagnetic devices based on changing the inductive impedance of a winding placed around a saturable magnetic core. This mechanism is achieved by changing the permeability of the magnetic material. As the saturation level of the magnetic material is increased, the operation point of the magnetic core is displaced on the material *B(H)* curve towards the maximum flux density. These devices, therefore, allow for additional degrees of freedom in the design and control of Power Electronic Converters (PECs) [1][2][3].

The main aspects regarding the construction of a Variable Inductor (VI) are strongly related to the selection of the core material since the magnetization curve as well as the hysteresis loop both differ in shape and characteristics with different magnetic materials [4]. However, the geometrical structure of the VI also plays an important role in its operation. Specifically, when scaling up to applications of high frequency or high power, some specifications such as symmetry, the coupling between the AC and DC windings, and the induced voltages become critical to study.

In a recent research direction for alternative core arrangements that provide symmetry in terms of AC and DC flux paths, many possibilities have been investigated, the most common of which are the double-E structure [4][5], the triple-E structure [6][7] and the quad-U structure [8][9]. The VI based on double-E structure is composed of two E cores stacked on top of each other to form three branches. The main winding is wound around the middle branch which is gapped to avoid quick saturation of the core, and the control windings are serially connected in opposite direction around the left and right branches [4]. The main drawback of this configuration is the asymmetrical distribution of AC and DC flux throughout the core [8][10]. The VI based on triple-E structure is composed of two E cores to implement the main AC winding of the inductor, and a third E core placed at the bottom part of the double-E cores to place the DC bias control windings. Some drawbacks are associated with the triple-E configuration, the most significant of which is the requirement to handle high bias current to achieve a sufficient variation of the inductance. This poses complications on the supplying circuits and elevates the losses [8]. The VI based on quad-U core consists of four U cores, they are arranged such that each two U cores are stacked on top of each other, and a vertical separator is inserted between each set of U cores to avoid any flux interaction between the sets [8]. The main advantage of the quad-U structure is that it has a symmetrical distribution of AC and DC flux paths, which is postulated to allow a larger inductance range variation for the same VI volume compared to the double-E and triple-E cores.

The previously mentioned structures are based on current-controlled concept [5], the most widely used for conventional VI. Though a voltage-controlled structure is also possible to construct a VI [11][12].

This work was supported by grant MCINN-22-TED2021-129796B-C21 and MCINN-23-PID2022-139479OB-C22 funded by MCIN/AEI /10.13039/501100011033. This work was partially funded from the EU H2020 R&I Program under grant agreement 864459 (Project “TALENT”) and through ERFD Structural Funds. This work was supported in part by the Spanish Ministry of Economy and Competitiveness funded by MCIN/AEI/10.13039/501100011033 under Grants MCINN-23-PID2022-139479OB-C22, MCINN-22-TED2021-129796B-C21, and in part by the European Union NextGenerationEU/PRTR. *(Corresponding author: Sarah Saeed).*

Sarah Saeed is with the University of Oviedo, Gijón, 33204 Spain (e-mail: saeedsarah@uniovi.es). Jorge García is with the University of Oviedo, Gijón, 33204 Spain (e-mail: garciajorge@uniovi.es). Color versions of one or more of the figures in this article are available online at http://ieeexplore.ieee.org

There is not a single topology that will be universally satisfactory, however, the proper selection of the magnetic regulator structure is strongly related to the application requirements. For this motivation, the paper presents an addition to the literature on this aspect by proposing a new structure for constructing a VI. The proposed structure is based on a toroid core shape modified to include a cut hole around which the auxiliary control windings are wound. The key contributions of this proposal are thus detailed as follows.

The first key contribution is the innovative structure which has been analyzed, constructed, characterized, and eventually proved to offer three main advantages compared to the existing ones. On one hand, the structure is based on a widely standardized core shape and is simple to construct. And, on the other hand, the proposed cut confines the control winding within its designed width, therefore shortening the DC flux path. Accordingly, even though there are mismatches between the reluctances of left and right control branches, the effect of such mismatches is drastically minimized in comparison with other available VI structures [10]. Thus, providing a symmetrical operation and a better decoupling of the DC control winding, and consequently low induced voltage in the control windings.

The latter characteristic, intrinsic to the proposed structure, allows for its use in high power applications, where previous studies have encountered serious problems related to induced voltage [13][14]. Thereafter, **the second key contribution** is employing the proposed VI to an electrochemical battery Energy Storage System (ESS). In addition to the variation of the inductance, the proposed structure offers a wide range of variation of the inherent series resistance, both features can be used as a degree of freedom to compensate for the change of the system parameters. This results in two main advantages: one regarding the battery health, and the other regarding the system controller, as clarified hereafter.

From one side, for most of the battery technologies available in the market, the voltage and current ripple through the battery imposes higher stress due to harmonics, which would cause an increased heat generation, uneven electrode wear, and potential degradation of the battery's active materials [15][16]. This implies that the ripple percentage should be minimized to fit within a design margin to mitigate its effects [17]. Using the variation of the inductance, it is possible to control the ripple without the need for installing extra capacitors to act as a high frequency filter.

And, from another side, as the State-Of-Charge (SOC) of the battery changes, its impedance will change as well. As the system controller is tuned using the system impedance parameters, then to keep the controlled system transient behavior within the designed range, the controller should be re-tuned, changing its parameters each time the battery charge/ discharge condition varies. Apart from being generally an unpractical solution, the change of the controller parameters requires a certain time delay which is due to the sampling period of the digital programmer and the precision of the sensors employed. Also step changes in the parameters would imply abrupt changes. For some critical battery chemistries, it is crucial for the battery State-Of-Health (SOH) to keep smooth and continuous variations in the voltage and current [15][18]. Having a magnetically controlled variable inductance assures this smooth non-stepped variation [19].

The third key contribution of the work is constructing a VI prototype based on the proposed structure, presenting its corresponding mathematical model, a step-by-step design example, as well as small and large signal characterization under different operation frequencies and saturation conditions. This is complemented with building a reduced scale ESS prototype to experimentally verify the applicability of the proposal by measuring some performance factors such as the efficiency, the temperature, and the induced voltage.

The paper is thus organized as follows. Section II presents the structure and main principle of operation of the VI. While the analytical modelling of the device is presented in detail in section III. Section IV shows a design example for the VI, showing the prototype constructed and the measured inductance variation. Section V provides a discussion on the main contributions of the proposed approach to the studied application. In this section, also the used battery module is characterized and modeled. The prototype was then employed in a DC/DC converter and the experimental results obtained are stated in section VI. Finally, section VII presents the conclusions of the work.

II. Proposed Symmetrical Toroid VI

The proposed toroidal VI structure is illustrated in Fig. 1. As can be seen, it consists of a toroid with a horizontal cut. The main AC winding (red) has a number of turns N_{ac} and is wound around the main toroid arm. The DC control windings (blue) are wound through the cut, around the two arms formed by this incision. Each of the DC windings has a number of turns N_{dc} and are serially connected in opposite polarity to allow the DC flux generated to add and flow in the closed path, as clarified by Fig. 2.

The horizontal cut is, therefore, meant to create the closed path for the DC flux that flows through the control windings and thus saturating only this small partition of the magnetic core as it will be explained in detail in the following section.

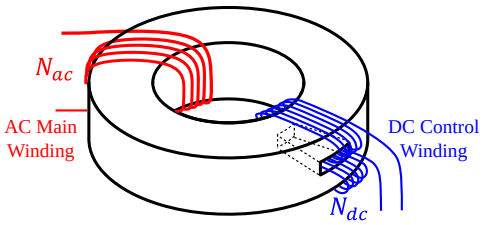

Fig. 1. Construction of the toroidal-cut variable inductor.

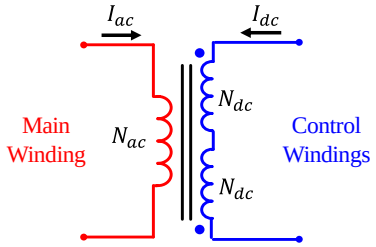

Fig. 2. Variable inductor main winding and control windings.

The DC flux will bias the operation on the *B(H)* curve of the magnetic material, causing this portion of the core to be controllably saturated. This DC bias will vary the permeability of the core causing the equivalent reluctance of the core to differ and thus varying the inductance value seen from the main winding.

The idea proposed is similar in concept to the principle of operation of the Virtual Air Gap (VAG). While most of the magnetic path remains unchanged, a local saturated region is generated, thus having a similar behavior to an air gap that can virtually vary its length [20]. In this context, an increase in the control current generates a higher reluctance at the intervened core section, in other words, an equivalent bigger air gap. Although the operation is similar to a VAG, it cannot be modeled in the same manner because in order to create a VAG the whole control winding is inserted within the magnetic core [21]. This creates three magnetic flux paths in such a way that the majority of the flux establishes between the orifices [22]. This is not the case in the proposed variable inductor topology, the structure proposed in this work is much simpler to construct. It is based on standard toroid cores, which are available in almost all sizes and magnetic materials and is easily manufactured. In the present work, the cut was done by direct drilling into the core with a twist drill bit. However, the core can also be constructed on a large-scale industrial level by using one of three techniques: automated drilling, premanufactured industrial molds, or 3D printing specifically additive manufacturing [23]. The latter technique has been widely tested for inductor production [23][24][25] and proven better thermal management. Moreover, on a small-scale research level, 3D commercial printers are also an alternative for constructing customized cores [26][27]. For both construction methods, the simplest and fastest structure which can be designed and printed is the toroidal core [28].

Some examples of industrial applications in which the proposed variable inductor topology can be employed are: Electro-Magnetic Interference (EMI) filters, battery chargers, electric vehicles, and solid-state transformers oriented to microgrid applications.

The detailed analysis and operation of the proposed variable inductor is explained in detail in the following section.

III. Analytical Modeling of the VI

There are two complementary aspects for modeling a magnetic device; one aspect is defining the behavior of the magnetic core material itself, and the other aspect is the identification of the electromagnetic behavior of the device in terms of the core geometry, winding arrangement, and the magnetomotive force (mmf) which represents the electric and magnetic interaction.

On the aspect of magnetic core material, in this work the relationship between the magnetic flux density, B, and the field intensity, H, is modeled using the anhysteresis curve [19]. The *B(H)* curve is intrinsic to the magnetic material and is extracted from the manufacturer as will be explained in detail in the following section.

On the aspect of the full electromagnetic system, the modeling methods are confined to either analytical or numerical methods. Specific to variable magnetic devices, modeling strategies are mainly [19]: Finite Element Analysis (FEA), gyrator-capacitor model, and reluctance equivalent circuit [4]. The latter being the one used for modelling the variable inductor in this work.

Fig. 3 shows the AC and DC windings of the toroidal VI and the corresponding flux distribution in the core. As can be observed an AC main flux, φ_{ac}, is generated due to the AC main winding (red) and flows through the whole core and splits to the two branches formed by the horizontal cut. The DC control windings (blue), on the other hand, generate a DC flux, φ_{dc}, which tends to flow through a short path closed by the branches formed due to the horizontal cut. This happens because the mean length of the control path is much shorter compared to the full toroid mean length, therefore presenting much lower magnetic reluctance.

The DC flux would bias the operation point of the magnetic core pushing it towards the knee of the *B(H)* curve, causing a variation of the magnetic permeability, which changes the equivalent reluctance of the core, and consequently varies the inductance seen from the main winding [14]. Detailed explanation and mathematical analysis are provided throughout this section and the following one.

Fig. 4 shows the equivalent reluctance circuit of the toroidal VI. The total flux in each of the branches: main, left, and right, are stated using (1), (2), and (3), respectively.

$$\varphi_M = \varphi_{ac} \tag{1}$$

$$\varphi_L = -\varphi_{dc} + \frac{\varphi_{ac}}{2} \tag{2}$$

$$\varphi_R = \varphi_{dc} + \frac{\varphi_{ac}}{2} \tag{3}$$

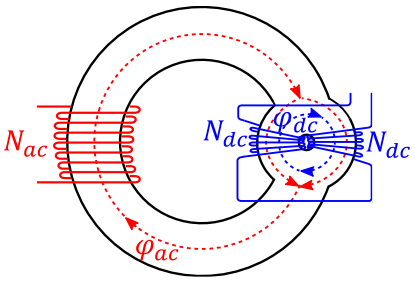

Fig. 3. Windings and flux distribution of the toroidal-cut variable inductor.

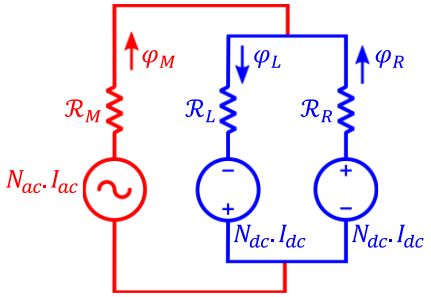

Fig. 4. Equivalent reluctance circuit of the toroidal-cut VI.

The reluctances of the different magnetic paths are calculated based on the length, l_i, cross-section area, A_i, and permeability, μ, of the corresponding magnetic path i.

The reluctance of the main path of the AC flux, $\mathcal{R}_M$, is calculated as shown in (4).

$$\mathcal{R}_M = \frac{l_M}{\mu \cdot A_M}, \tag{4}$$

where A_M is the cross-section area of the toroid, l_M is the length of the reluctance path of the main branch, and μ is the permeability of the magnetic material. While the reluctances of the left and right control paths of the DC flux, $\mathcal{R}_L$ and $\mathcal{R}_R$, are calculated as shown in (5) and (6), respectively [4][29].

$$\mathcal{R}_L = \frac{l_L}{\mu \cdot A_L}, \tag{5}$$

$$\mathcal{R}_R = \frac{l_R}{\mu \cdot A_R}, \tag{6}$$

where A_L and A_R are the cross-section areas of the left and right branches, respectively, and l_L and l_R are the lengths of the reluctance paths of the left and right control branches, respectively.

Due to the cut in the toroidal core, the cross-section area of the control branches is less than half that of the main branch. Fig. 5 illustrates the calculations of the cross-section areas of the different magnetic paths in the toroid. The depth of the cut is defined by δ, the width of the toroid is *w*, and its height is *h*. For more clarification, the equations to calculate the cross-section areas A_M, A_L and A_R are shown in (7) and (8).

$$A_M = w \times h, \tag{7}$$

$$A_L = A_R = w \times \frac{h-\delta}{2}, \tag{8}$$

Based on the equivalent reluctance circuit, the inductance value seen from the main winding can be expressed as shown in (9).

$$L = \frac{{N_{ac}}^2}{\mathcal{R}_M + \left(\frac{\mathcal{R}_L \cdot \mathcal{R}_R}{\mathcal{R}_L + \mathcal{R}_R}\right)} \tag{9}$$

Assuming symmetry of the left and right control branches, i.e. $\mathcal{R}_L = \mathcal{R}_R$, the latter equation can be simplified to (10).

$$L = \frac{{N_{ac}}^2}{\mathcal{R}_M + \frac{\mathcal{R}_L}{2}} \tag{10}$$

On the other hand, the inductance seen from the control windings can be calculated in a similar manner as shown in (11).

$$L_{dc} = \frac{{N_{dc}}^2}{\mathcal{R}_L + \mathcal{R}_R} = \frac{{N_{dc}}^2}{2\,\mathcal{R}_L} \tag{11}$$

As conceived from the previous discussion, and similar to most VI structures, in the proposed one the AC flux also goes through the DC windings in an opposite manner to avoid excessive reflected AC voltage across the bias winding [8]. Nevertheless, considering only this assumption, as it is in the case of the double-E core among others, would ensure acceptable reflected voltage only within a certain range of operation. However, going to higher power and voltage levels, those induced voltages would rapidly build up exceeding the acceptable limits. Such excessive voltage would complicate the design of the DC control windings and implicate careful design of turn-to-turn isolation and current capacity rating. This makes the double-E core, among other conventional structures, not applicable for high power applications.

The proposed technique thus extends beyond this, by shortening the DC flux path. This would imply that even if there are mismatches in the flux between left and right branches, which translate into a mismatch between the reluctance of one path and the other, these are much smaller compared to the conventional double-E core VI, for example. In this latter configuration, the DC flux circulates all the circumference of the core, therefore, the right and left branches would have significantly larger path lengths implicating a much bigger mismatch between reluctances [10].

Apart from this, EE and EI structures, in general, present nonlinear distribution of the permeability values across the core; under saturation conditions, some parts of the magnetic core, specifically the corner points, are not utilized or in other words unsaturated [10]. However, in the case of toroid cores, this is not observed. For this reason, as well, the proposed structure targets using a toroid core that would present symmetrical operation and save unused magnetic material [10].

IV. Design Example of the Toroid VI

A. Design and construction

The selected iron powder material is -52 material from MICROMETALS [30]. This material it has low core losses at high frequency, and has an initial permeability, μ_i, of 75. The inductor is built using the toroid T225A-52B part from MICROMETALS [30], whose modified shape and construction is illustrated in Fig. 6. The corresponding dimensions of the core are listed in Table I.

The design specifications of the power converter are stated in Table II. Based on these specifications, the nominal inductance value that satisfies the requirements is calculated as shown in (12) to be 620 µH.

$$L = \frac{P}{2\pi f \cdot \Delta i_{ac} \cdot {I_p}^2} \tag{12}$$

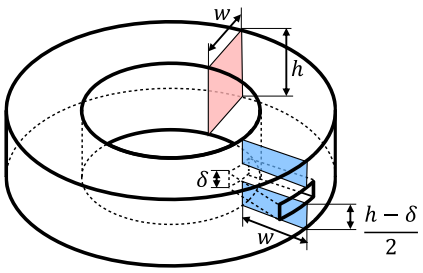

Fig. 5. Cross-section areas of the AC and DC branches of the toroidal-cut variable inductor.

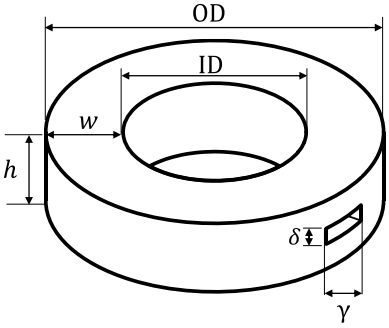

Fig. 6. Shape and core dimensions of the proposed toroid core.

TABLE I
CORE DIMENSIONS AND RELUCTANCE PATH LENGTHS

Equivalent length of the core	l_e	146 mm
Outer diameter	OD	57.15 mm
Inner diameter	ID	35.69 mm
Height of the core	h	25.4 mm
Width of the core	$w = \frac{OD - ID}{2}$	10.73 mm
Width of the cut	δ	5 mm
Length of the cut	γ	20 mm
Lengths of the reluctance paths of the left or right control branches	$l_L = l_R \approx \gamma$	20 mm
Length of the reluctance path of the main branch	$l_M = l_e - \gamma$	126 mm

TABLE II
SPECIFICATIONS OF THE POWER CONVERTER

Power, *P*	2 kW
Input voltage, V_{in}	0 – 200 V
Switching frequency, *f*	20 kHz
Inductor peak current, I_p	10 A
Ripple current, Δi_{ac}	10%
Temperature	25ºC – 70ºC

The number of turns of the main winding, N_{ac}, as well as the control windings, N_{dc}, are selected based on the target operation point of the magnetic material. To understand this, the material permeability as well as *B(H)* curves are modeled.

The permeability variation as a function of the magnetic field intensity, *H*, in Oersted units, is given by the expression (13).

$$\mu = \left(\frac{1}{a + b \cdot H^c} + d\right) \cdot \mu_i / 100 \,, \tag{13}$$

where $a=1.00e^{-2}$, $b=4.66e^{-6}$, $c=1.84$, and $d=0$, which are constants specific to the magnetic material [30], and μ_i is the initial permeability which has a value of 75 specific to the powder material -52 [30]. Fig. 7 shows the permeability curve as a function of the H_{DC}.

The magnetic flux density, *B*, in Gauss units, as a function of the field intensity, *H*, in Oersted units, is given by the expression (14).

$$B(H) = \frac{\mu_i}{\frac{1}{H + aH^b} + \frac{1}{cH^d} + \frac{1}{e}}, \tag{14}$$

where $a=1.67e^{-1}$, $b=2.02$, $c=1.09e^{2}$, $d=2.55e^{-1}$, and $e=2.47e^{2}$, which are constants specific to the magnetic material [30]. Fig. 8 shows characteristic *B(H)* curve of the material.

The operation region on the *B(H)* curve is selected around the knee of the curve in order to provide the variation of the magnetic material permeability, related to the slope of the *B(H)* curve, and consequently a variable inductance. The magnetic field intensity can be designed within the range of 4000 – 20000 A/m. As mentioned previously, only the partition of the core with the DC control windings will be saturated, the rest of the core will always be operated in the linear region of the *B(H)* curve. Based on this, the AC field intensity, H_{AC}, would have a maximum value of 4000 A/m. While the DC field intensity, H_{DC}, would have a maximum of 20000 A/m.

Based on the AC and DC field intensities, the number of turns of the AC main winding and the DC control windings can be calculated, respectively, as explained by (15) and (16).

$$H_{AC} = \frac{N_{ac} I_{ac}}{l_M}, N_{ac} = \frac{H_{AC} \cdot l_M}{I_{ac}} = \frac{4000 \times 12.6e^{-2}}{10} \approx 60\ turns \tag{15}$$

$$H_{DC} = \frac{N_{dc} I_{dc}}{l_R}, N_{dc} = \frac{H_{DC} \cdot l_R}{I_{dc}} = \frac{20000 \times 2.0e^{-2}}{2} \approx 200\ turns \tag{16}$$

The selected wire diameters and the rest of the design specifications are summarized in Table III. Fig. 9 illustrates the constructed variable inductor.

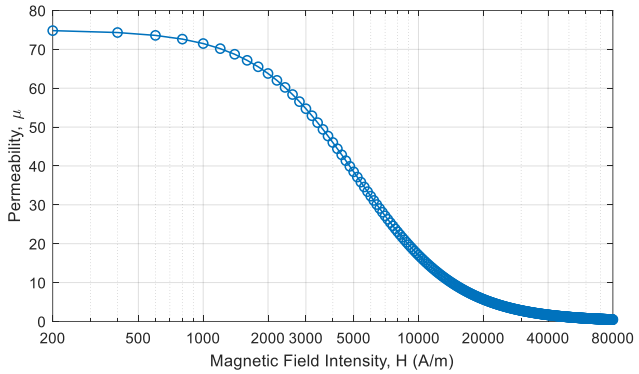

Fig. 7. Permeability of iron powder magnetic material -52 [30].

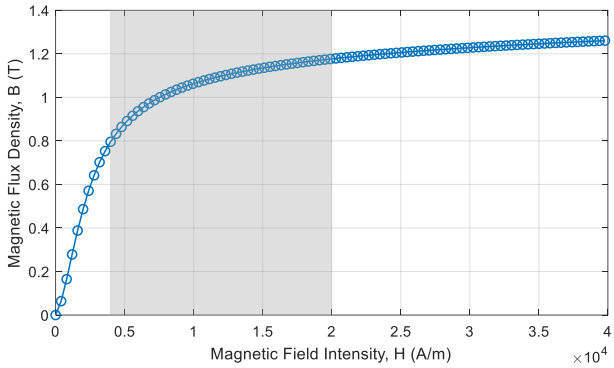

Fig. 8. *B(H)* curve of iron powder magnetic material -52 [30].

TABLE III
SPECIFICATIONS OF VARIABLE INDUCTOR PROTOTYPE

Core size and material	T225A-52B
Inductance factor, A_L	155 nH
Inductance variation range, L_{max} - L_{min}	620 µH to 510 µH
No. of turns of main winding, N_{ac}	60 turns, 1.6 mm
No. of turns of control winding, N_{dc}	200 turns, 0.3 mm

Fig. 9. The constructed variable inductor based on the toroidal-cut magnetic core.

The cut width, δ, and its length, γ, are done as a function of the core geometry such that the required number of turns of the DC bias windings can be fit through its depth. In this design, the wire diameter of the control winding, D_{dc}, is selected to be 0.3 mm, and each of the left and right windings are wound in 3 layers, therefore the cut length and width are calculated as shown in (17) and (18), respectively.

$$\gamma \geq \frac{N_{dc}}{3} \cdot D_{dc} \tag{17}$$

$$\delta \geq 3 \cdot D_{dc} \tag{18}$$

It is worth noting that the length of the cut in this design example is around 14% of the equivalent core length and should be constrained to a maximum of 20% to maintain a relatively short DC flux path.

Moreover, to calculate the inductance of the control windings, the reluctance of the left or right control branch is calculated. And using (11), L_{dc} is calculated to be 3.5 mH.

B. Testing under small signal analysis

The experimental inductor variation range and sensibility has been tested by applying a DC control current, I_{dc}, through the control windings of the variable inductor. Then, the inductance seen from the main winding was measured using the impedance analyzer Agilent Technologies E5061B.

Fig. 10 shows the total measured inductance seen from the DC control winding as a function of the frequency. Moreover, Fig. 11 shows the measured inductance and the series resistance seen from the main winding as a function of the frequency for different values of bias control current, highlighting the frequency of operation at 20 kHz.

As can be observed the inductance value reduces from around 620 µH to 510 µH when the control current is varied from 0 to 2 A. This fulfills the design specifications stated in the previous section. The series resistance of the inductor shows a decreasing trend as well as a function of the control current, as further explained in Fig. 12.

It is worth noting that, for the battery application in hand, the objective is to maintain a relatively small variation of the inductance, i.e. approximately a flat curve, with a total of 100 µH variation compared to the nominal value of 620 µH, while allowing for a relatively wide variation of the series resistance.

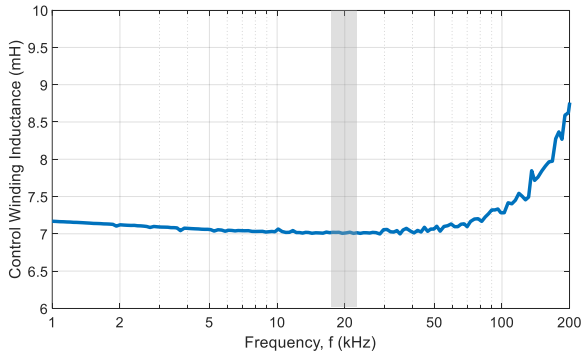

Fig. 10. The total measured inductance seen from the DC control windings as a function of the frequency.

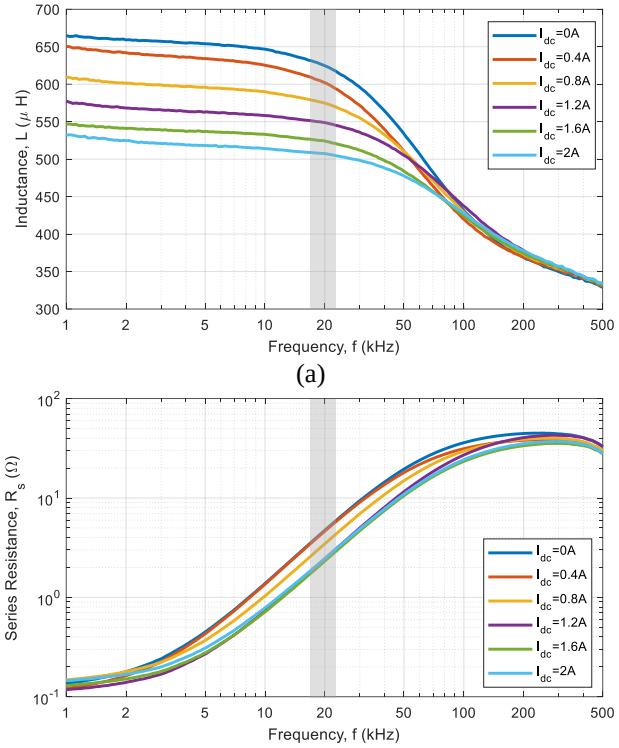

Fig. 11. (a) Measured inductance seen from the main winding, and (b) series resistance, as a function of the frequency for different values of bias control current. The obtained measurements at the operation frequency of 20 kHz are highlighted.

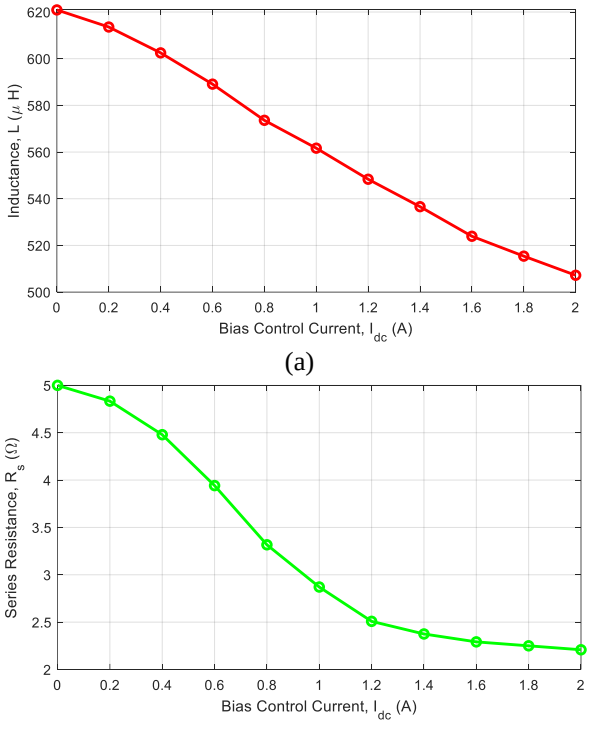

Fig. 12. Measurements obtained by the impedance analyzer for different values of the bias control current at the operation frequency of 20 kHz, (a) measured inductance and (b) series resistance.

V. Comparative Analysis

The variable inductor structure based on the toroid cut core has been analyzed, designed, constructed, and characterized in the previous sections. To complement the study, in this section a review is realized for the relevant existing VI topologies, which can thereby serve as a brief guide for selecting the suitable VI structure on the basis of the application requirements.

Table IV summarizes the merits and demerits of the different VI structures reviewed. It also lists the most popular applications that were reported in literature using those topologies. In addition, a quantitative comparative analysis between different VI structures is illustrated in Fig. 13, where the aspects of comparison are the power range, the control current and the size. The obtained comparison values are relative and expressed in p.u. values [19]. More comparison aspects such as the characteristics of the inductance curve as a function of DC bias current can be found in [10][14].

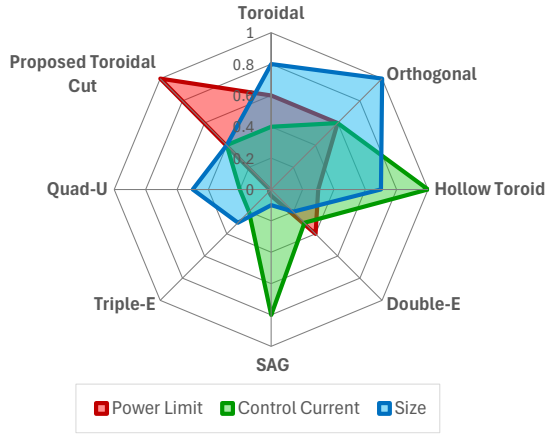

Fig. 13. Quantitative comparative analysis of different variable inductor structures.

VI. Application of the Proposed Variable Inductor to Battery Energy Storage System

The proposed variable inductor topology is studied within a bidirectional boost converter used to interface and control the current through a battery ESS. The circuit diagram of the converter is shown in Fig. 14. The battery ESS module intended for this application is composed of one string of 4 Lithium-ion cells connected in series, Fig. 15(a). The investigated cell is an 18650-sized high-energy round cell with a nominal capacity of 2.6 Ah and a nominal cell voltage of 3.7 V. The battery stack is built using 4 modules with configurable output terminals which are connected in series depending on the required system voltage level, Fig. 15(b). The Battery Management System (BMS) used to monitor and record the cell voltage and temperature is bq76PL455EVM from Texas instruments.

The impedance model of the battery is shown in Fig. 16. The model is based on Thevenin equivalent, and its parameters are obtained experimentally from the battery response to a step in the current as explained hereafter [41][42][43].

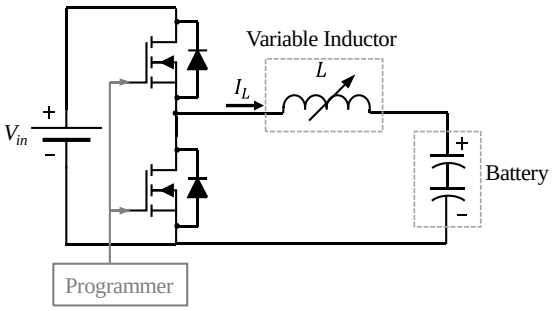

Fig. 14. Circuit diagram of the bidirectional boost converter used to integrate battery energy storage system into DC grid.

TABLE IV
Variable Inductor Structures and Applications

VI Topology	Merits	Demerits	Application	Typical Power Limit	Typical Control Current	Typical Converter Efficiency
Toroidal [31][32][33]	-Standard core shape. -Simple construction.	-Induced AC voltage in DC windings specially as bias current increases.	-Telecommunication. -AC regulation. -High current such as welding machines.	3 kW	2 A	86%
Orthogonal [34][35]	-Harmonics reduction related to SVC.	-Small inductance variation range. -Extra filtering required.	-Reactive power compensation.	3 kW	3 A	87%
Hollow Toroid [36]	-Reduced effect on AC main circuit.	-High bias current. -Complicated mathematical modelling.	-Resonant converters. -EMI filters.	1.5 kW	5 A	not reported
Double-E [4][5][37]	-Symmetrical structure. -Relative simplicity and versatility. -Low bias current.	-Nonlinear coupling between AC and DC windings. -Relatively high induced voltage in control windings.	-Induction heaters. -Resonant converters. -Contactless power transfer. -Electronic ballast. -SST. -EV.	2 kW	1.5 A	94%
SAG [38][39][40]	-Progressive saturation independent of magnetic material permeability.	-Unconventional manufacturing of core.	-Active PFC.	200 W	4 A	not reported
Triple-E [6]	-Permeability modulated within a small portion of the core.	-Handles high bias current. -Complicated supply circuit.	-LED driver.	100 W	1 A	91%
Quad-U [8]	-Symmetrical distribution of AC and DC fluxes. -Large inductance variation range.	-More complicated analysis to solve AC and DC operation separately.	-LED driver. -Fluorescent lamp driver.	50 W	1 A	93%
Proposed Toroidal Cut	-Symmetrical structure and distribution of AC and DC fluxes. -Low induced voltage in control windings. -Large series resistance variation range. -Based on widely standard toroid cores.	-Requires adaptation of standard cores (using automated drilling, molds, or 3D printing).	-EMI filters. -Interfacing ESS. -High power applications.	≥ 5 kW	2 A	96%

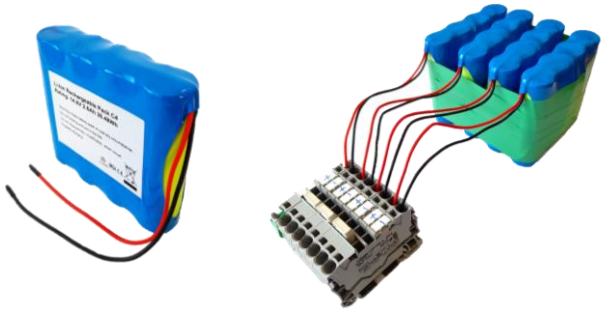

(a) (b)

Fig. 15. Tested Lithium-ion battery, (a) battery module composed of 4 Lithium-ion cells in series, and (b) battery stack composed of 4 modules connected in series with configurable terminals.

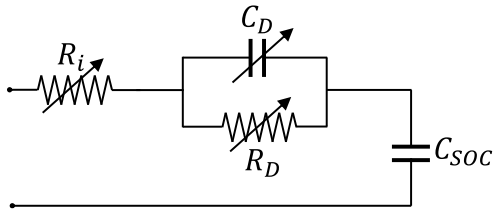

Fig. 16. Battery impedance model [38][40].

TABLE V
MEASURED BATTERY PARAMETERS

Parameter	Value
R_i	40 mΩ
R_D	85 mΩ
C_D	5 F
C_{SOC}	10 kF

Fig. 17 illustrates the test results during charging a battery cell at 1C. The test was carried out for a new battery cell at an ambient temperature of 25ºC and a current step from 0 A to 2.6 A. The battery response to the current step is recorded as highlighted in the plots in Fig. 17. Then the battery model parameters are calculated as summarized in Table V.

At steady state high frequency operation, the impedance of the battery cell can be approximated by its internal series resistance, R_i. The internal resistance of the used battery cell is calculated as a function of the SOC using the results from the cell discharge test at different rates. Fig. 18 shows the discharge test at 0.2C. To calculate R_i, the cell voltage is observed at the same cell capacity for different discharge rates, as illustrated in Fig. 19. R_i is, therefore, calculated as the change in voltage over the change in current at the same cell capacity [44]. The calculation is carried out by considering the change from one discharge rate to another.

The calculated R_i curves using different discharge rates are depicted in Fig. 20 as a function of the SOC. It can be observed that the internal resistance increases as the SOC increases [45]. Moreover, the resistance of the full battery module is illustrated in Fig. 21 by taking the mean value of the obtained curves and assuming the four cells in series having similar resistance curves. The internal resistance suffers the most variation between 60% to 100% SOC, where its value increases from 0.2 Ω to 1 Ω approximately.

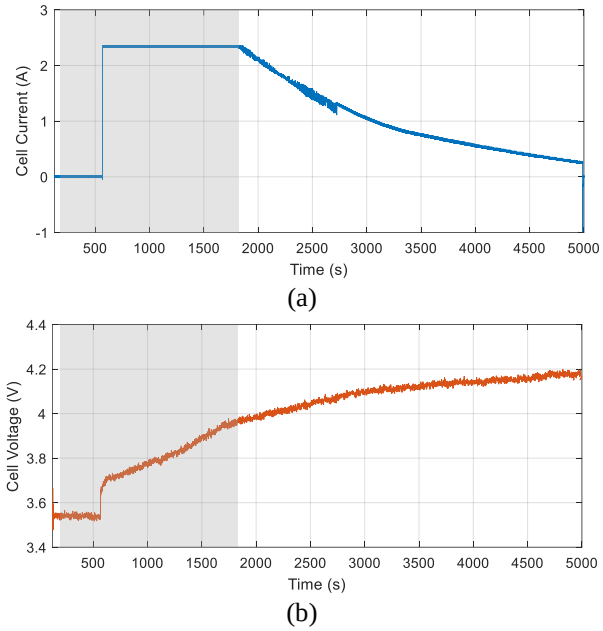

Fig. 17. Experimental results of battery cell charge at 1C. (a) Cell current, and (b) cell voltage.

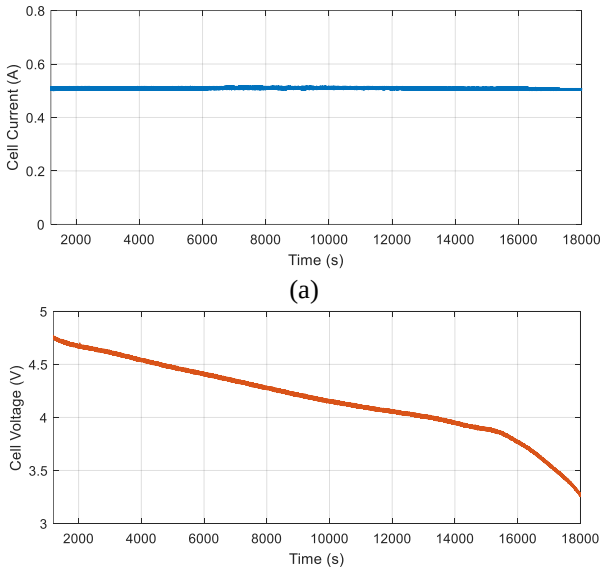

Fig. 18. Experimental results of battery cell discharge at 0.2C. (a) Measured cell current, (b) measured cell voltage.

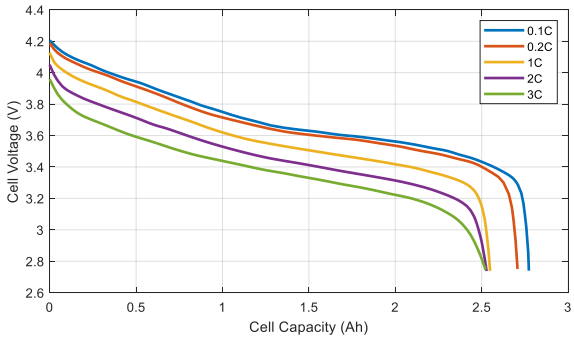

Fig. 19. Battery cell discharge test illustrating cell voltage as a function of its capacity at different discharge rates.

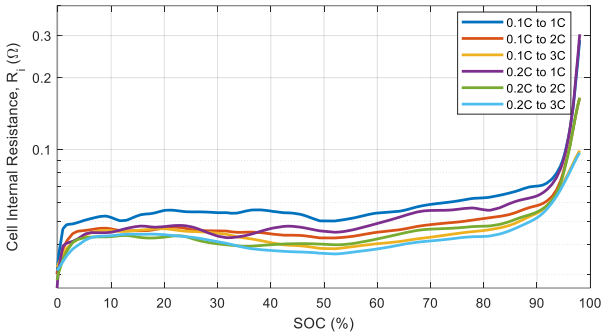

Fig. 20. Internal resistance as a function of SOC analyzed at different cell capacities.

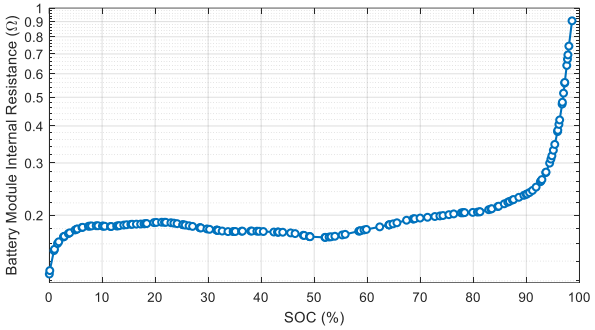

Fig. 21. Internal resistance as a function of SOC for the full battery module formed of four cells in series.

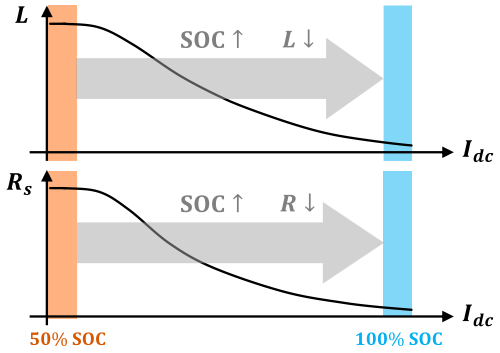

Fig. 22. Proposed variable inductor operation as a function of the battery SOC.

Specific to this application, an increase in the battery SOC, especially in the range between 60% to 100% SOC, would mean an increase in the module impedance in the range of 1 Ω for one battery module and 4 Ω when using the four modules in series. Consequently, the voltage ripple would be significantly amplified [45].

Another way to control such ripple is by means of the switching frequency. However, using a variable frequency implies complicating the converter design on several aspects such as the design of passive elements, EMI issues, system losses, among others [4][46], so, it is considered an intrusive technique. While, on the other hand, using the inductance variation is a passive technique because it modifies the system equivalent impedance without affecting the battery impedance nor the operation parameters of the converter.

The proposed operation can be further clarified by Fig. 22. Assuming the lowest battery SOC is 50% and the highest is 100%, then whenever the SOC increases, the variable inductor value is decreased, i.e. the operation point is moved to the right on the illustrated curves. Therefore, the series resistance decreases as well. This would eventually allow for controlling the increasing voltage ripple.

Furthermore, the change in the module internal resistance would also mean a change in the system equivalent impedance which would affect the controller behavior, calling for a continuous change in gains, and consequently affecting the overall performance of the power converter [45]. In some cases, depending on the converter topology and the input and output voltage levels, even a relatively small variation of the internal battery resistance (in range of mΩ) would cause a significant change in the current level. The variable inductor can thus be used to restore the equivalent resistance to the design value by decreasing or increasing its series resistance based on the point of saturation, as can be observed in Fig. 11.

Based on this analysis, the proposed variable inductor topology can provide a potential parameter to control the voltage and current ripple in an energy storage system. Thus, avoiding battery stress due to harmonics, without the need for installing bulk oversized capacitors in parallel with the battery terminals, or allowing to reduce their size significantly.

VII. Experimental Results

A. Experimental test setup

As explained in the previous sections, the novel variable inductor proposed structure will be tested in a bidirectional boost converter used to integrate battery ESS in DC grid applications. Fig. 23 shows the converter topology and the connection of the variable inductor. Also, Fig. 24 illustrates the prototype used for the tests.

The power stage is composed of a commercial mother board provided by GaN Systems [47]. The board can be equipped with up to two half-bridge modules, each consisting of two GS66516B GaN transistors. The transistor is bottom-side cooled, rated at 650V/25mΩ, typically used in high efficiency applications [47]. As illustrated in Fig. 24, the modules are constructed using metal core PCB to cool GaN bottom-side cooled power transistors. The driver board is mounted on top of the PCB of the transistors, such that it provides a compact two-board assembly. The programmer used to provide the Pulse Width Modulated (PWM) signals to the board is based on the Texas Instruments TMS320F28335 Digital Signal Processor (DSP). The power supply used is Electro-Automatik EA-PS 9750-12, which is regenerative to allow for charging and discharging the battery. Table VI summarizes the specifications of the test setup.

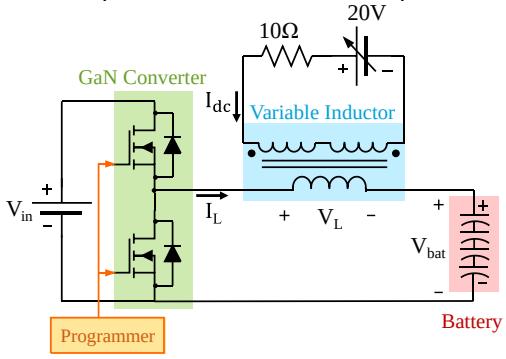

Fig. 23. Circuit diagram of the test platform.

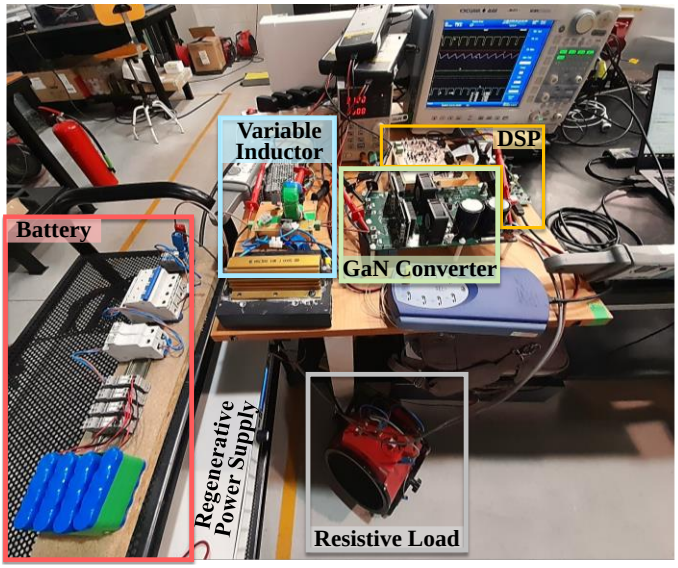

Fig. 24. Experimental test setup.

TABLE VI
SPECIFICATIONS OF TEST SETUP

Converter	
Topology	Half bridge
GaN module	GSP65R13HB-EVB
Commercial converter	GSP65MB-EVB
Programmer	
DSP board	TMS320F28335 controlCARD
Variable Inductor	
Core size	T225A-52
Inductance variation range, ΔL	620 µH to 510 µH
Operation Conditions	
Input voltage, V_{in}	0 – 200 V
Switching frequency, f	20 kHz
Inductor peak current	10 A
Temperature	25ºC – 60ºC

B. Experiments using the battery impedance model

As mentioned during the previous sections, the proposed variable inductor topology is used mainly to restore the voltage ripple in the battery under changing SOC. During the tests, the bidirectional boost converter is operated at 0.8 duty cycle and the nominal frequency of 20 kHz.

Experimental tests are carried out to verify the viability of the proposed symmetrical variable inductor structure based on toroidal-cut magnetic core. During these initial experiments, the impedance model of the battery is used and not the battery itself. As the model of the battery at steady state is approximated by its internal resistance, then the load in this case is a resistive load.

Assuming a battery SOC of 100% and charging at 3C, the voltage drop in the total internal series resistance of the full battery stack (approximately 4 Ω in addition to the resistance of the connection cables) is estimated to be in the range of 50V. While charging a battery, this voltage drop would add up to its open circuit voltage so the estimated output voltage would reach almost 120V. Using a duty ratio of 0.8, the input voltage is thus adjusted to 150V to replicate this battery stack condition.

It is worth noting that, though in the following sections the experiments using the battery stack are illustrated, the initial choice of the use of the battery impedance model (not the battery stack itself) was to test at extreme SOC conditions without having to fully discharge or charge the battery each time the test is carried out. This was an essential approach to be able to test the viability of the proposed idea in a simplified manner.

Fig. 25(a) illustrates the converter switching waveforms at 100% SOC. A high SOC implicates higher battery internal resistance, and, in this case, the maximum battery voltage ripple can be observed. Furthermore, Fig. 25(b) shows the use of the variable inductor to compensate for the high resistance value and, consequently, reduce the voltage ripple. As observed by the measurement cursors, the variation of the inductance achieves around 10% reduction of the battery voltage ripple.

It is worth noting that, for such applications, the variable inductor should be designed based on the battery impedance characteristics for the targeted operation range.

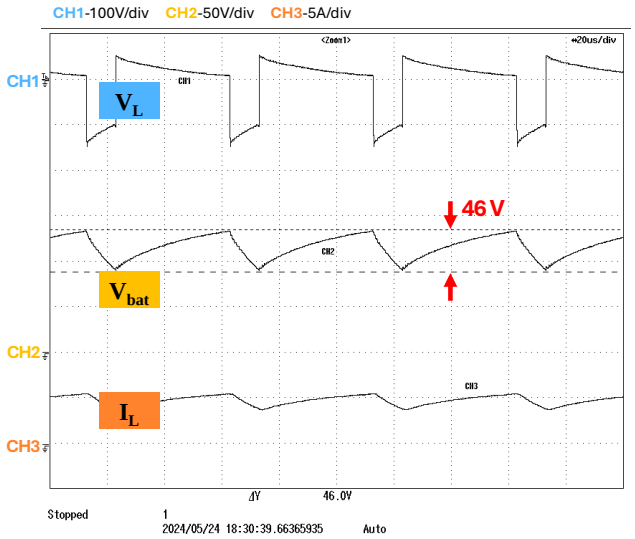

(a)

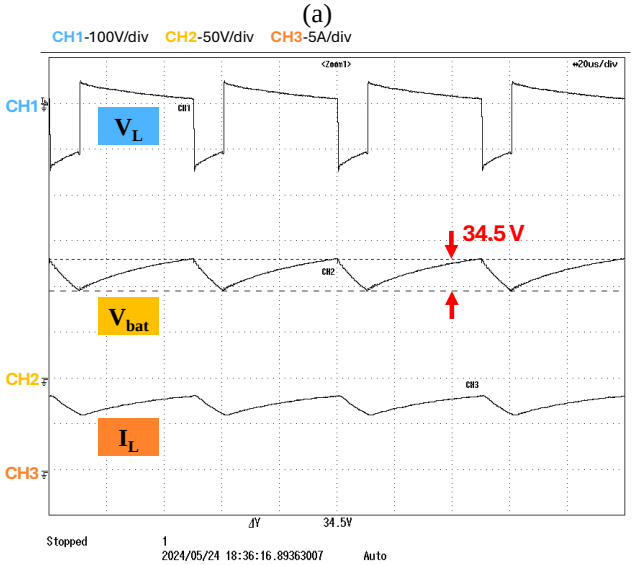

(b)

Fig. 25. Experimental results using battery impedance model at 20kHz, with 0.8 duty cycle at V_{in}=150V, and a battery SOC of 100%. Illustrating the switching waveforms of the converter charging 4 battery modules. (a) Fixed inductance, and (b) internal resistance compensation using variable inductor.

C. *Experiments using the battery ESS stack*

During this section, the full battery stack, composed of 4 modules connected in series, undergoes charging at different rates while applying the variable inductance to control the current ripple in the inductance.

In Fig. 26, an oscilloscope screen capture illustrates the results of the inductance variation from minimum to maximum value while charging the battery stack at 2C. Moreover, to illustrate the converter switching waveforms, a zoom is captured at each of the latter inductance values. For obtaining the minimum inductance value, the control current is set to the maximum, I_{dc}=2A, so the inductance value is 510 µH. The switching waveforms corresponding to this case are illustrated in Fig. 27(a). Similarly, another zoom is captured at the maximum inductance value, obtained by setting I_{dc}=0A so that the inductance value is 620 µH, as illustrated in Fig. 27(b).

As observed by the measurement cursors, the variation of the inductance value affects the current ripple; the ripple in the first case is 1.22A while in the second it is 1A. Therefore, the variation of the inductance achieves around 22% reduction of the current ripple that is charging the battery.

D. *Overall converter efficiency and losses breakdown*

To evaluate the overall converter efficiency, experimental tests are carried out to charge the full battery stack at different rates ranging from 0.5C to 3.5C. For the sake of demonstration of obtained sample results, Fig. 28 shows the converter switching waveforms at 3 different rates, 1C, 2C, and 3C.

As can be observed, these latter tests correspond to an average inductor current of 2.6 A, 5.2 A, and 7.8 A, respectively. The variation of the charging rate is achieved by changing the level of the input voltage, as seen in the figure.

The input and output power of every stage of the converter is computed by multiplying the measured average voltage and current at that stage. Therefore, the power losses corresponding to the different converter components are determined, and in turn the efficiency. In this context, Fig. 29(a) shows the obtained efficiency curve as a function of the battery charging rate.

The efficiency value is seen to approach a maximum of 96.6% at 2.5C, which corresponds to an average inductor current of 6.5 A. After which the efficiency value slightly drops at higher rates.

To clarify the obtained values, Fig. 29(b) depicts a p.u. power loss breakdown among all the converter components; namely: switches' losses, inductor losses, bias winding losses, and cooling system losses. It is worth noting that the losses of the bias winding and the cooling system are accounted for at their maximum possible values.

It is quite interesting to observe the evolution of the power losses of the different converter components with respect to the overall losses. For example, the switches' losses are decreasing with the increase of the current because the converter is approaching its rated current, while the inductor losses are increasing due to the increased copper losses.

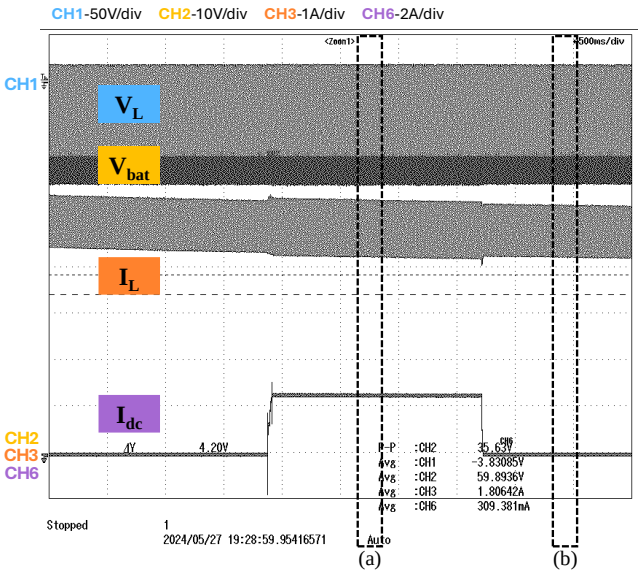

Fig. 26. Experimental results using battery stack. Illustrating converter waveforms during charging battery stack at a rate of 2C, while changing the DC bias current in a step between minimum and maximum values.

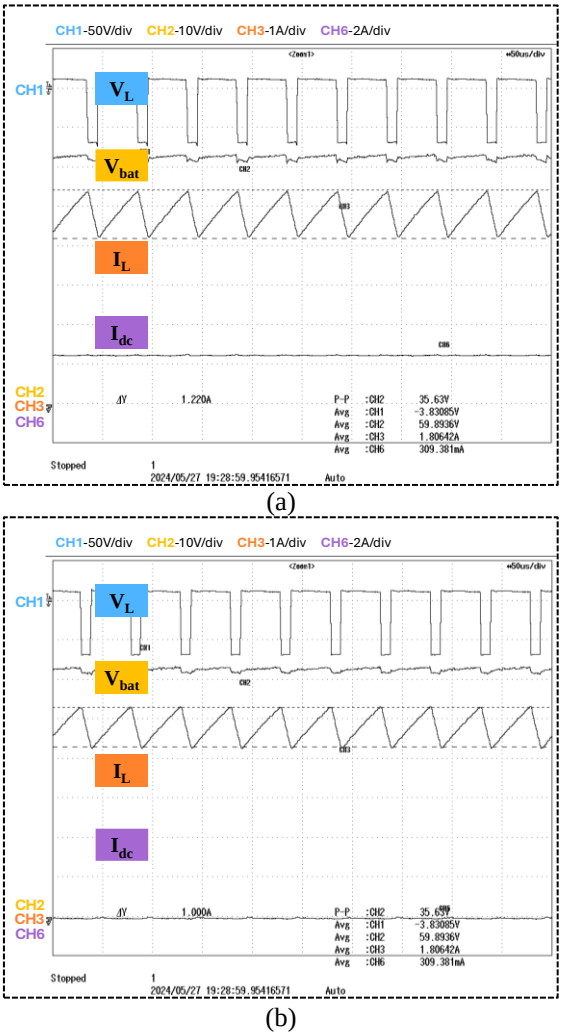

Fig. 27. Experimental results using battery stack. Zoom illustrating the switching waveforms at: (a) I_{dc}=2A and L=510µH, and (b) I_{dc}=0A and L=620µH.

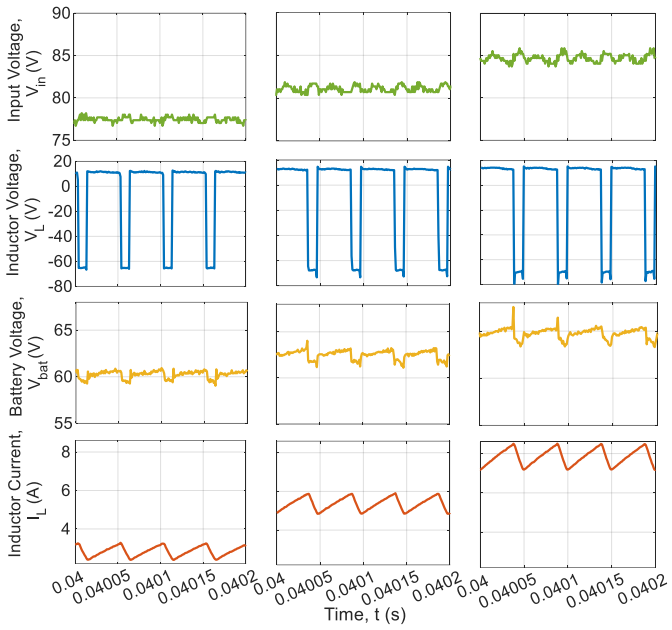

(a) (b) (c)

Fig. 28. Experimental results using battery stack. Illustrating the switching waveforms during charging at: (a) 1C, (b) 2C, (c) 3C.

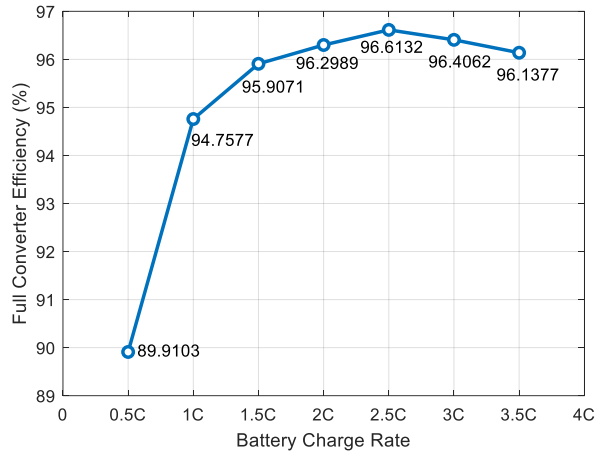

(a)

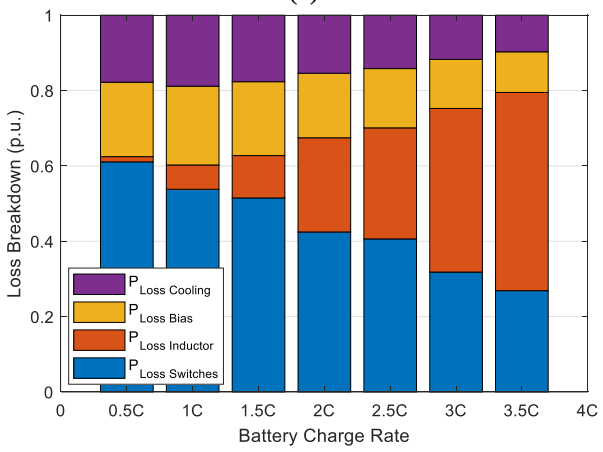

(b)

Fig. 29. Experimental results using battery stack, (a) efficiency curve of the full converter, and (b) p.u. maximum power losses breakdown including all converter components, at different battery charging rates.

E. Induced voltage in DC bias winding

Moreover, as mentioned previously, among the advantages of the proposed VI structure is decoupling the DC flux from the AC one, and thus reducing the induced voltage in the bias windings. To validate this, the temperature of the magnetic core is measured during the converter operation. The results are illustrated in Fig. 30.

The measurement is repeated for the two extreme conditions of saturation mentioned previously, at 0 A and 2 A of control current, while the converter is operating at 150 V input voltage. It can be observed that, in the case of minimum saturation point, i.e. at 0 A, the maximum temperature measured in the variable inductor was located on the main winding and is recorded to be 35.3º. While in the case of the maximum saturation point, i.e. at 2 A, the maximum temperature measured in the variable inductor was located on the control winding and is recorded to be 41.2º.

Additionally, the induced voltage in the control windings has been measured at the maximum saturation point, I_{dc} = 2 A, for different levels of input voltage. The resulting values are shown in Fig. 31.

It can be observed that the induced voltages in the windings are fluctuating between a minimum of 7 V to a maximum of 11 V for the full range of input voltage operation. The maximum percentage of induced voltage that was recorded is around 7%. This is considered a very reduced induced voltage in the control windings compared to other studied variable inductor topologies, which have reported multiples of this percentage during the coupling between the main winding and the control winding [4][5][10][19][48]-[50].

(a)

(b)

Fig. 30. Variable inductor measured temperature at an input voltage of 150V, for two conditions of saturation: (a) no saturation, I_{dc}=0A, and (b) maximum saturation, I_{dc}=2A.

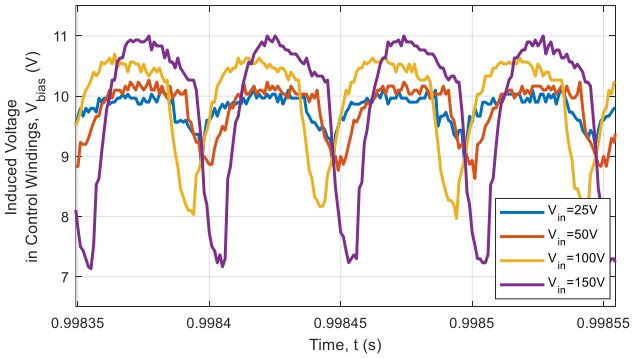

Fig. 31. Induced voltage in the control windings at 2 A bias current, for different input voltage levels.

VIII. Conclusions

The contributions of the work cover two main aspects: the first is proposing an original variable inductor structure that is an added opportunity to the ones available in the known literature which could expand the range of applicability of variable inductors to high-frequency high-power switching converter applications. And the second is tackling some applications that could benefit from the specific characteristics provided by this proposed structure; applications which specifically require a continuous variation of the inductance or wide variation of the series resistance.

Regarding the first aspect, the variable inductor based on a cut toroidal core was analytically modeled, a design example was provided, constructed, and characterized under small-signal as well as large-signal analysis using a laboratory prototype based on GaN switches. Moreover, the proposed variable inductor structure was compared to the widely used EE and EL structures and found to provide some crucial advantages such as the symmetry in AC and DC flux, and thereby a reduced voltage reflected through the control windings.

Regarding the second aspect, the application studied is the use of the variable inductor in the current control for charging and discharging a Lithium-ion battery stack, which is a novel proposal. In this context, the work presented the characterization of the battery cell under test, the elaboration of the relationship between SOC and internal resistance, as well as the use of the variable inductor to compensate the change in the system parameters and thereby control the ripple through the battery. This contributes to avoiding battery aging as well as maintaining the control system transient behavior as designed.

Moreover, to test the viability of the proposed variable inductor structure, the efficiency and the loss breakdown among the different components of the full system were calculated based on experimental results at different charging rates. An interesting future development would be to compare the obtained efficiency values with those of the converter counterparts.

Although the setup elaborated for this work is a reduced scale prototype, scaling up to higher frequency and higher power levels would result in further advantage to the use of the proposed variable inductor structure compared to other conventional ones which have limited applicability due to reflected voltage in the DC windings. The aim of this work is to validate the principal idea, with the potential for undertaking higher frequency in future developments.

In addition to this, the study can be further extended by implementing a real time estimation method for the battery internal resistance, similar to the one presented in [51]. In that manner, instantaneous feedback can be provided to the variable inductor control system.

It is worth noting that the proposed approach is valid for Lithium-ion batteries. For other types of battery chemistries and other battery capacities, the design and operation of the variable inductor would require further study.

References

[1] C. S. Buitrago, D. B. Cobaleda and W. Martinez, "Magnetically Controlled Transformer With Variable Turns Ratio and Low Series Inductance: Analysis and Implementation Toward Its Application in SMPS," in IEEE Transactions on Power Electronics, vol. 38, no. 11, pp. 14360-14374, Nov. 2023, doi: 10.1109/TPEL.2023.3300583.

[2] Y. Wu, C. Deng, S. Roy and A. J. Hanson, "A Communication-less Wireless Battery Charger Based on Variable Inductor," 2024 IEEE Applied Power Electronics Conference and Exposition (APEC), Long Beach, CA, USA, 2024, pp. 296-301, doi: 10.1109/APEC48139.2024.10509481.

[3] X. Zhu et al., "High-Efficiency WPT System for CC/CV Charging Based on Double-Half-Bridge Inverter Topology With Variable Inductors," in IEEE Transactions on Power Electronics, vol. 37, no. 2, pp. 2437-2448, Feb. 2022, doi: 10.1109/TPEL.2021.3107461.

[4] M. S. Perdigão, M. F. Menke, Á. R. Seidel, R. A. Pinto and J. M. Alonso, "A Review on Variable Inductors and Variable Transformers: Applications to Lighting Drivers," in IEEE Transactions on Industry Applications, vol. 52, no. 1, pp. 531-547, Jan.-Feb. 2016, doi: 10.1109/TIA.2015.2483580.

[5] D. Medini and S. Ben-Yaakov, "A current-controlled variable-inductor for high frequency resonant power circuits," *Proceedings of 1994 IEEE Applied Power Electronics Conference and Exposition - ASPEC'94*, Orlando, FL, USA, 1994, pp. 219-225 vol.1, doi: 10.1109/APEC.1994.316396.

[6] Y. Hu, L. Huber, and M. M. Jovanovic, "Single-stage, universal-input AC/DC led driver with current-controlled variable PFC boost inductor," IEEE Transactions on Power Electronics, vol. 27, no. 3, pp. 1579-1588, 2012.

[7] E. A. Bitencourt, M. R. Cosetin, I. G. Vegner, and R. N. do Prado, "A ferromagnetic based variable inductor analysis and design methodology," in 2015 IEEE 13th Brazilian Power Electronics Conference and 1st Southern Power Electronics Conference (COBEP/SPEC), 2015, pp. 1-5.

[8] J. M. Alonso, M. Perdigão, M. A. Dalla Costa, S. Zhang, and Y. Wang, "Analysis and experimentation of the quad-U variable inductor for power electronics applications," IET Power Electronics, vol. 11, no. 14, pp. 2330-2337, 2018.

[9] U. Boeke, "Scalable Fuorescent lamp driver using magnetic amplifers," in 2005 European Conference on Power Electronics and Applications, 2005, pp. 10 pp.-P.10.

[10] S. Saeed, J. Garcia, M. S. Perdigão, V. S. Costa, B. Baptista and A. M. S. Mendes, "Improved Inductance Calculation in Variable Power Inductors by Adjustment of the Reluctance Model Through Magnetic Path Analysis," in *IEEE Transactions on Industry Applications*, vol. 57, no. 2, pp. 1572-1587, March-April 2021, doi: 10.1109/TIA.2020.3047593.

[11] M. Liserre *et al.*, "Voltage Controlled Magnetic Components for Power Electronics," in *IEEE Power Electronics Magazine*, vol. 10, no. 2, pp. 40-48, June 2023, doi: 10.1109/MPEL.2023.3273892.

[12] S. Choi, J. -W. Shin, J. Imaoka and M. Yamamoto, "Voltage-Controlled Variable Inductor for Fixed-Frequency Critical Conduction Mode Operation," in IEEE Transactions on Industrial Electronics, vol. 70, no. 6, pp. 5707-5716, June 2023, doi: 10.1109/TIE.2022.3198235.

[13] S. Zurek, J. Hall, T. Kutrowski and A. Cheer, "Experimental Verification of 2.4 kVAr and 12 kVAr Prototype Variable Inductors Controlled By Virtual Air Gaps With Magnetic Orthogonality," in IEEE Transactions on

Power Delivery, vol. 37, no. 6, pp. 4880-4887, Dec. 2022, doi: 10.1109/TPWRD.2022.3162174.

[14] M. M. S. D. Perdigão, "Research and development on new control techniques for electronic ballasts based on magnetic regulators," Ph.D. dissertation, University of Coimbra, Sept. 2012.

[15] "Lithium-Ion Batteries: Science and Technologies" edited by Masaki Yoshio, Ralph J. Brodd, and Akiya Kozawa

[16] Z. Xia and J. A. Abu Qahouq, "State-of-Charge Balancing of Lithium-Ion Batteries With State-of-Health Awareness Capability," in IEEE Transactions on Industry Applications, vol. 57, no. 1, pp. 673-684, Jan.-Feb. 2021, doi: 10.1109/TIA.2020.3029755.

[17] S. De Breucker, "Impact of dc-dc Converters on Li-ion Batteries," Ph.D. dissertation, Katholieke Universiteit Leuven, Leuven, Belgium, Dec. 12, 2012.

[18] L. Lu, X. Han, J. Li, J. Hua, and M. Ouyang, "A review on the key issues for lithium-ion battery management in electric vehicles," Journal of Power Sources, vol. 226, pp. 272–288, 2013. [Online]. Available: http://www.sciencedirect.com/science/article/pii/S0378775312016163.

[19] Sarah Saeed, "Contributions to the Design, Operation, and Control of DAB Bidirectional Converters Based on Variable Magnetic Elements", Ph.D. dissertation, University of Oviedo, Spain, June 2020.

[20] V. Molcrette, J. -. Kotny, J. -. Swan and J. -. Brudny, "Reduction of inrush current in single-phase transformer using virtual air gap technique," in IEEE Transactions on Magnetics, vol. 34, no. 4, pp. 1192-1194, July 1998, doi: 10.1109/20.706479.

[21] Jean-Francois Brudny, Guillaume Parent, Ines Naceur. Characterization and Modeling of a Virtual Air Gap by Means of a Reluctance Network. IEEE Transactions on Magnetics, 2017, 53 (7), pp.8002007.10.1109/TMAG.2017.2680402 . hal-03350733f

[22] A. Konrad and J. F. Brudny, "An improved method for virtual air gap length computation," in IEEE Transactions on Magnetics, vol. 41, no. 10, pp. 4051-4053, Oct. 2005, doi: 10.1109/TMAG.2005.854987.

[23] Y. Yan, J. Moss, K. D. T. Ngo, Y. Mei, and G. Lu, "Additive manufacturing of toroid inductor for power electronics applications," IEEE Trans. Ind. Appl., vol. 53, no. 6, pp. 5709–5714, Nov./Dec. 2017, doi: 10.1109/TIA.2017.2729504.

[24] C. Ding, S. Lu, L. Liu, K. D. T. Ngo, and G. -Q. Lu, "Additive manufacturing of hetero-magnetic coupled inductors," IEEE Trans. Compon. Packag. Manuf. Technol., vol. 11, no. 6, pp. 1028–1034, Jun. 2021, doi: 10.1109/TCPMT.2021.3083179.

[25] L. Liu, T. Ge, K. D. T. Ngo, Y. Mei, and G.-Q. Lu, "Ferrite paste cured with ultraviolet light for additive manufacturing of magnetic components for power electronics," IEEE Magn. Lett., vol. 9, 2018, Art. no. 5102705.

[26] Selema, Ahmed & Ibrahim, Mohamed & Sergeant, Peter. (2023). Advanced Manufacturability of Electrical Machine Architecture through 3D Printing Technology. Machines. 11. 10.3390/machines11090900.

[27] W. Liang, L. Raymond, and J. Rivas, "3-D-Printed Air-Core Inductors for High-Frequency Power Converters," IEEE Transactions on Power Electronics, vol. 31, no. 1, pp. 52-64, 2016.

[28] F. Corti et al., "Evaluation of Additive Manufacturing for Wireless Power Transfer Applications," in IEEE Transactions on Industrial Electronics, vol. 71, no. 5, pp. 4586-4595, May 2024, doi: 10.1109/TIE.2023.3283679.

[29] J. M. Alonso, M. Perdigão, M. A. Dalla Costa, S. Zhang and Y. Wang, "Variable inductor modeling revisited: The analytical approach," 2017 IEEE Energy Conversion Congress and Exposition (ECCE), Cincinnati, OH, USA, 2017, pp. 895-902, doi: 10.1109/ECCE.2017.8095880.

[30] MICROMETALS IRON POWDER CORE CATALOG 2022. [Online]. Available: https://www.micrometals.com/design-and-applications/literature/.

[31] A. S. Kislovski, "Quasi-linear controllable inductor," in *Proceedings of the IEEE*, vol. 75, no. 2, pp. 267-269, Feb. 1987, doi: 10.1109/PROC.1987.13731.

[32] M. W. Beraki, J. P. F. Trovão, M. S. Perdigão and M. R. Dubois, "Variable Inductor Based Bidirectional DC–DC Converter for Electric Vehicles," in IEEE Transactions on Vehicular Technology, vol. 66, no. 10, pp. 8764-8772, Oct. 2017, doi: 10.1109/TVT.2017.2710262.

[33] A. P. Mendes, B. Baptista, M. S. Perdigão and A. M. S. Mendes, "Experimental analysis of a DC current-controlled variable inductor in a DC-DC converter," 2019 IEEE International Conference on Industrial Technology (ICIT), Melbourne, VIC, Australia, 2019, pp. 440-445, doi: 10.1109/ICIT.2019.8755161.

[34] O. Ichinokura, T. Jinzenji and K. Tajima, "A new variable inductor for VAR compensation," in *IEEE Transactions on Magnetics*, vol. 29, no. 6, pp. 3225-3227, Nov. 1993, doi: 10.1109/20.281144.

[35] O. Ichinokura, K. Tajima and T. Jinzenji, "Study of push-pull parametric transformer," in IEEE Transactions on Magnetics, vol. 28, no. 5, pp. 2181-2183, Sept. 1992, doi: 10.1109/20.179436.

[36] H. Wouters, C. Suarez and W. Martinez, "Orthogonal Biasing Controllable Inductor using a Commercial Hollow Toroid Core," 2023 11th International Conference on Power Electronics and ECCE Asia (ICPE 2023 - ECCE Asia), Jeju Island, Korea, Republic of, 2023, pp. 294-300, doi: 10.23919/ICPE2023-ECCEAsia54778.2023.10213978.

[37] S. Saeed, J. Garcia and R. Georgious, "Dual-Active-Bridge Isolated DC–DC Converter With Variable Inductor for Wide Load Range Operation," in *IEEE Transactions on Power Electronics*, vol. 36, no. 7, pp. 8028-8043, July 2021, doi: 10.1109/TPEL.2020.3048928.

[38] W. H. Wolfle and W. G. Hurley, "Quasi-active power factor correction with a variable inductive filter: theory, design and practice," in *IEEE Transactions on Power Electronics*, vol. 18, no. 1, pp. 248-255, Jan. 2003, doi: 10.1109/TPEL.2002.807135.

[39] W. Wolfle, W. G. Hurley and S. Lambert, "Quasi-active power factor correction: the role of variable inductance," 2001 IEEE 32nd Annual Power Electronics Specialists Conference (IEEE Cat. No.01CH37230), Vancouver, BC, Canada, 2001, pp. 2078-2083 vol. 4, doi: 10.1109/PESC.2001.954427.

[40] L. Zhang, W. G. Hurley and W. H. Wölfle, "A New Approach to Achieve Maximum Power Point Tracking for PV System With a Variable Inductor," in IEEE Transactions on Power Electronics, vol. 26, no. 4, pp. 1031-1037, April 2011, doi: 10.1109/TPEL.2010.2089644.

[41] Yoon-Ho Kim and Hoi-Doo Ha, "Design of interface circuits with electrical battery models," in IEEE Transactions on Industrial Electronics, vol. 44, no. 1, pp. 81-86, Feb. 1997, doi: 10.1109/41.557502.

[42] B. Schweighofer, K. M. Raab and G. Brasseur, "Modeling of high power automotive batteries by the use of an automated test system," IEEE Transactions on Instrumentation and Measurement, vol. 52, no. 4, pp. 1087-1091, Aug. 2003.

[43] A. R. Sparacino, G. F. Reed, R. J. Kerestes, B. M. Grainger and Z. T. Smith, "Survey of battery energy storage systems and modeling techniques," 2012 IEEE Power and Energy Society General Meeting, San Diego, CA, USA, 2012, pp. 1-8, doi: 10.1109/PESGM.2012.6345071.

[44] M. H. Hung, C. H. Lin, L. C. Lee and C. M. Wang, "State-of-charge and state-of-health estimation for lithium-ion batteries based on dynamic impedance technique," Journal of Power Sources, vol. 268, pp. 861-873, Dec. 2014.

[45] P. García, S. Saeed, Á. Navarro-Rodríguez, J. Garcia and H. Schneider, "Switching Frequency Optimization for a Solid State Transformer With Energy Storage Capabilities," in IEEE Transactions on Industry Applications, vol. 54, no. 6, pp. 6223-6233, Nov.-Dec. 2018, doi: 10.1109/TIA.2018.2860561.

[46] M. S. Perdigão, B. Baptista, H. Marques, E. S. Saraiva and J. M. Alonso, "On the use of magnetic regulators in electronic ballasts," 45th International Universities Power Engineering Conference UPEC2010, Cardiff, Wales, 2010, pp. 1-6.

[47] GaN Systems Inc. Technical Manual, "High Power IMS Evaluation Platform", Available in: https://gansystems.com/wp-content/uploads/2018/01/GSP65RXXHBEVBUserGuiderev20171219.pdf

[48] Y. Hu, L. Huber and M. M. Jovanović, "Single-Stage, Universal-Input AC/DC LED Driver With Current-Controlled Variable PFC Boost Inductor," in *IEEE Transactions on Power Electronics*, vol. 27, no. 3, pp. 1579-1588, March 2012, doi: 10.1109/TPEL.2010.2082564.

[49] E. Rozanov and S. Ben-Yaakov, "Analysis of current-controlled inductors by new SPICE behavioral model," HAIT Journal of Science and Engineering B, vol. 2, issues 3-4, pp. 558-570, 2005.

[50] M. Gulko, D. Medini and S. Ben-Yaakov, "Inductor-controlled current-sourcing resonant inverter and its application as a high pressure discharge lamp driver," *Proceedings of 1994 IEEE Applied Power Electronics Conference and Exposition - ASPEC'94*, Orlando, FL, USA, 1994, pp. 434-440 vol.1, doi: 10.1109/APEC.1994.316366.

[51] C. G. Moral et al., "Battery internal resistance estimation using a battery balancing system based on switched capacitors," 2019 IEEE Energy Conversion Congress and Exposition (ECCE), Baltimore, MD, USA, 2019, pp. 2516-2522, doi: 10.1109/ECCE.2019.8912675.